Supplementary information
Twist-angle dependent dehybridization of momentum-indirect excitons in $MoSe_2/MoS_2$ heterostructures

Nikodem Sokolowski[1], Swaroop Palai[1], Mateusz Dyksik[2], Katarzyna Posmyk[1,2], Michał Baranowski[2], Alessandro Surrente[2], Duncan Maude[1], Felix Carrascoso[3], Onur Cakiroglu[3], Estrella Sanchez[3], Alina Schubert[3], Carmen Munuera[3], Takashi Taniguchi[4], Kenji Watanabe[5], Joakim Hagel[6], Samuel Brem[7], Andres Castellanos-Gomez[3], Ermin Malic[6,7], Paulina Plochocka[1,2]

[1] Laboratoire National des Champs Magnétiques Intenses, UPR 3228, CNRS-UGA-UPS-INSA, Grenoble and Toulouse, France
[2] Department of Experimental Physics, Faculty of Fundamental Problems of Technology, Wroclaw University of Science and Technology, Wroclaw, Poland
[3] Materials Science Factory, Instituto de Ciencia de Materiales de Madrid (ICMM-CSIC), Madrid, E-28049, Spain
[4] International Center for Materials Nanoarchitectonics, National Institute for Materials Science, Tsukuba, Ibaraki 305-004, Japan
[5] Research Center for Functional Materials, National Institute for Materials Science, Tsukuba, Ibaraki 305-004, Japan
[6] Department of Physics, Chalmers University of Technology, 412 96 Gothenburg, Sweden
[7] Department of Physics, Philipps University of Marburg, 35037 Marburg, Germany

E-mail: paulina.plochocka@lncmi.cnrs.fr

Submitted to: *2D Mater.*

1. List of the samples

In our article, we investigated six samples of hBN-encapsulated $MoSe_2/MoS_2$ heterostructure denoted as A-F. Microscope images of the samples are provided in section 2. All samples' twist angles were determined and presented in section 3. The corresponding twist angle of each sample is given in Table S1.

Table S1. Sample Parameters List of the samples and corresponding twist angle.

	Twist angle (°)
Sample A	57.2
Sample B	0.4
Sample C	2.4
Sample D	56.3
Sample E	53.6
Sample F	6.4

2. Microscope images of the heterostructures

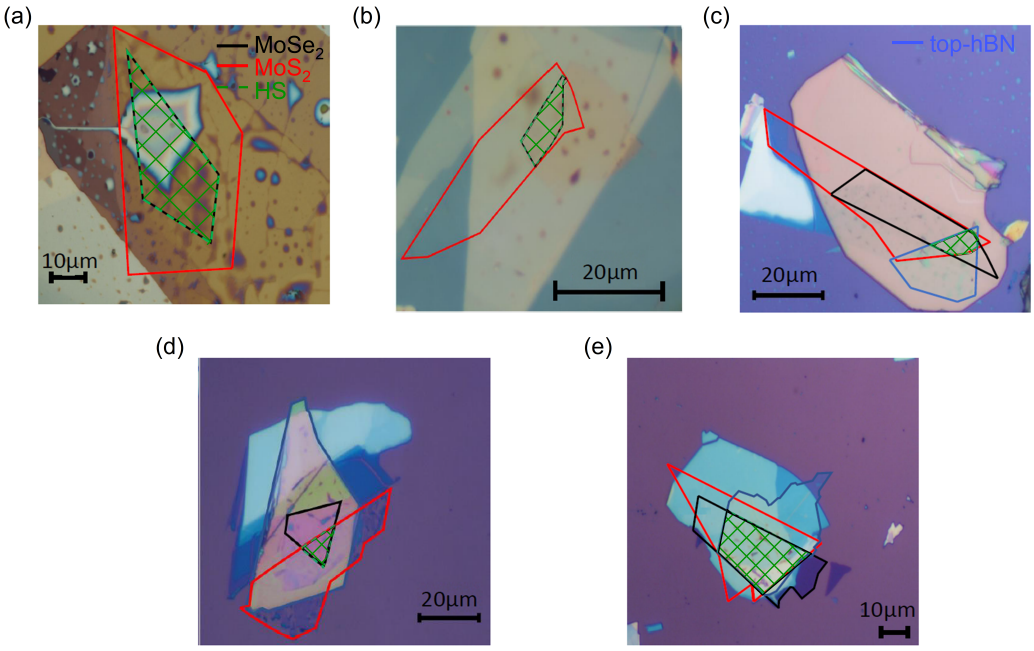

Figure S1. Microscope image of (a) Sample B, (b) Sample C, (c) Sample D, (d) Sample E, and (e) Sample F.

Fig. S1 shows an optical microscope image of the studied samples. The samples are $MoSe_2/MoS_2$ heterostructures encapsulated in hBN. $MoSe_2$ and MoS_2 monolayer flakes are indicated by the black and red lines, respectively. The overlap of the monolayers

($MoSe_2/MoS_2$ heterostructure) is indicated by the green dashed line with chequered pattern. For sample B, all measurements are performed outside the bubble area.

3. Second Harmonic Generation

Information about interlayer twist angle can be obtained by measuring polarization-resolved second harmonic generation (SHG) [1]. The system has a three-fold symmetry, which in linearly polarized SH dependence exhibits six-fold rotation symmetry. The obtained results can be successfully fit by the formula $I_{||}(2\omega) \propto \cos^2 3\phi$. For samples A, D-F, to fit better the results, the formula was modified by adding an extra term related to strain $\propto B\cos^2(2\theta + \phi)$ [2]. The twist angles are calculated as $|\phi_{MoSe_2} - \phi_{MoS_2}|$ or $2 \cdot |\phi_{monolayer} - \phi_{HS}|$. To determine if the interlayer twist angle is closer to 0° or 60°, one can compare the relative intensity of SHG between a monolayer and an HS. A more intense SHG signal on the HS than on the monolayer results from the constructive interference of the SHG generated in each monolayer. This is the signature of a tilted angle between the monolayer of 0°, whereas a weaker SHG intensity of HS corresponds to 60° [1].

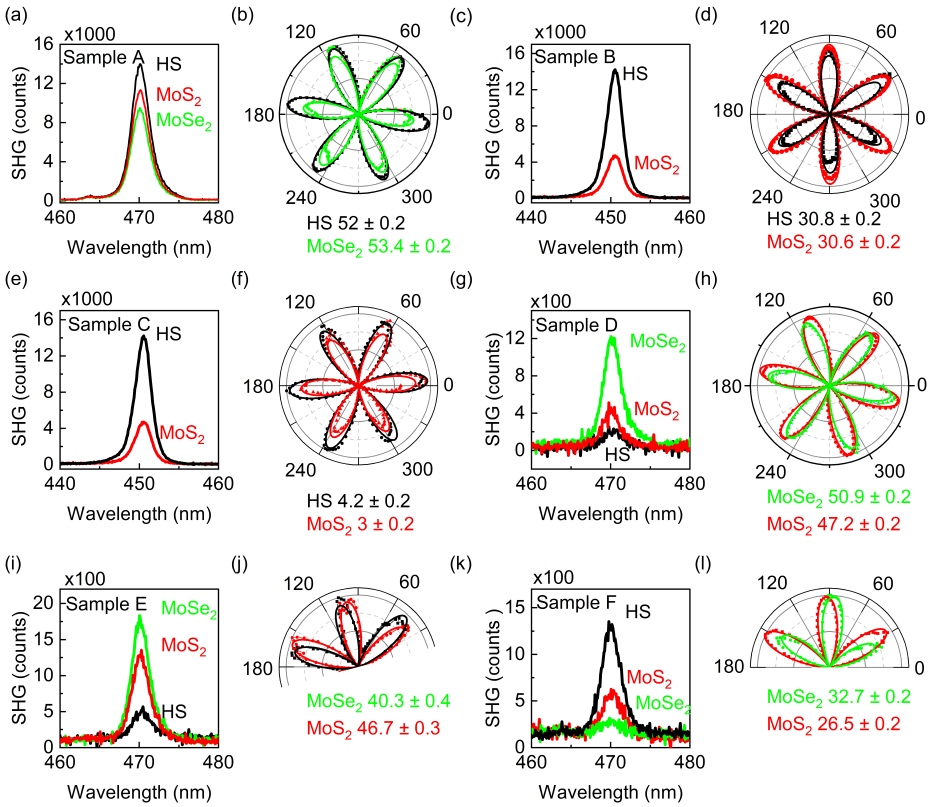

Figure S2. (a),(c),(e),(g),(i),(k) Intensity of second harmonic signal of monolayers and HS and (b),(d),(f),(h),(j),(l) corresponding polarization-resolved SHG.

4. Evolution of IX peak energy *versus* laser power

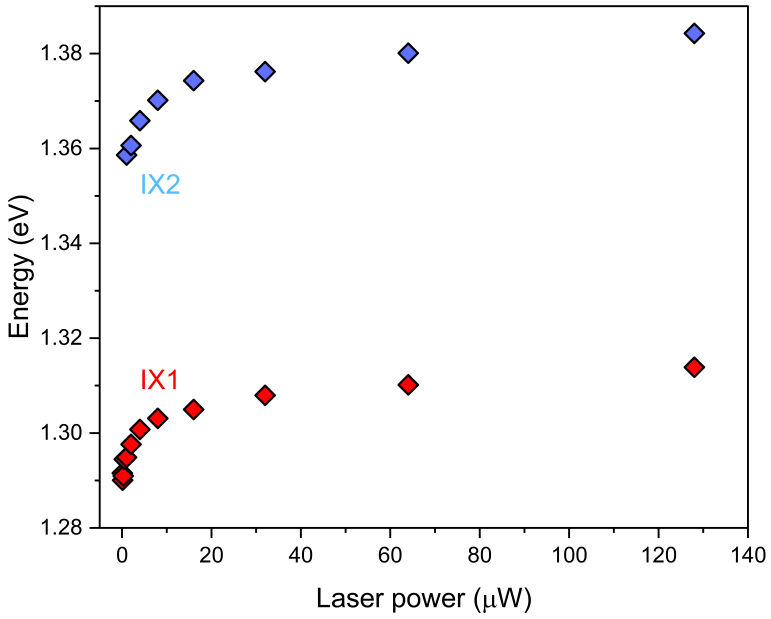

Figure S3. IX1 and IX2 energies as a function of the laser power, obtained from the same fitting procedure as in Fig. 5(a) of the main text.

5. Temperature-dependent photoluminescence of interlayer excitons

With increasing temperature, we observed that IX2-related emission quenches faster when compared with IX1 (Fig. S4 (a)). We determined the intensity of both IX1 and IX2 in Fig. S4 (b) and plot it in the form of an Arrhenius plot. By modeling the experimental data with the Arrhenius formula i.e.

$$I(T) = \frac{I_0}{1 + g_1 \exp(-\frac{E_1}{k_B T}) + g_2 \exp(-\frac{E_2}{k_B T})} \tag{1}$$

where E_1 and E_2 are the activation energies, I_0 is the initial intensity, g_1 and g_2 are the amplitude parameters, and k_B is the Boltzman constant. The determined activation energies for IX2 emission ($E_1 = 2.5\,\text{meV}$, $E_2 = 11.6\,\text{meV}$) are lower than the respective values for IX1 ($E_1 = 3.1\,\text{meV}$, $E_2 = 20.3\,\text{meV}$).

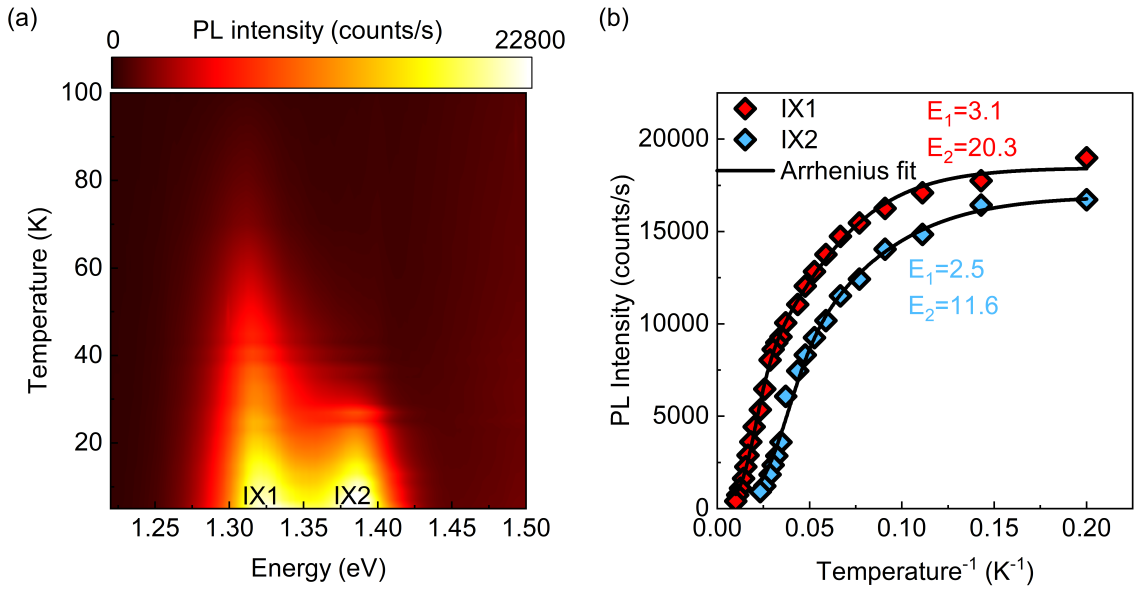

Figure S4. (a) Temperature-dependent PL data for sample B presented in the form of a false-color map. (b) Arrhenius plot of PL intensity both for IX1 and IX2. Solid lines are fits using Eq. 1

6. Theory

The most important factor which contributes to the tunneling strength is the stacking-dependent interlayer distance, which directly impacts the wavefunction overlap [3, 4]. As shown in Fig. S5(a), the tunneling strength is approximately linear with respect to the interlayer distance when considering the range of interlayer distance we have in the supercell [3]. Since the stacking configuration changes throughout the superlattice, the interlayer distance will also change. Consequently, we have a periodic tunneling strength throughout the superlattice [3, 5], as can be seen from Fig. S5(b).

Importantly, in Ref. [3] it is shown that the variation of the interlayer distance in the supercell becomes less pronounced with increased twist angle. Furthermore, the shortest interlayer distance becomes longer with increasing twist angle, in turn decreasing its tunneling strength due to the reduced wavefunction overlap. This decrease in the interlayer distance variation is approximately Gaussian and will effectively suppress the periodic modulation of the tunneling strength [3]. Due to the linearity between interlayer distance and tunneling, we can directly model the tunneling strength, where its periodic modulation is suppressed at higher twist angles. In this work, we do this by considering the same approach as in [5, 6], where the smoothly varying potential is modeled by interpolating between known values at the high symmetry stackings

$$t = t_0 + \left[\alpha + \beta e^{i2\pi/3}\right] \sum_{n=0}^{2} e^{i\boldsymbol{g}_n \cdot \boldsymbol{r}}, \tag{2}$$

where the parameters t_0, α and β are fitted to meet the condition at the high symmetry stackings.

In accordance with Ref. [3], we now let the periodic variation of the tunneling strength decrease as a Gaussian and converge to some specific value at large twist angles, thus modifying Eq. (2) to become twist angle dependent

$$t_{l_\lambda l'_\lambda}^{\lambda\xi_\lambda}(\boldsymbol{r}) = t^\lambda(d_{max}) + e^{-\theta^2/\theta_0^2}\Big(t_0^{\lambda\xi_\lambda} + \Big[\alpha^{\lambda\xi_\lambda} + \beta^{\lambda\xi_\lambda}e^{i2\pi/3}\Big]\sum_{n=0}^{2} e^{i\boldsymbol{g}_n\cdot\boldsymbol{r}}\Big). \tag{3}$$

Here, $t^\lambda(d_{max})$ is the tunneling strength that is present when the periodic modulation has disappeared at large twist angles. In this work, this is taken to be were the interlayer distance is the largest, which corresponds to the tunneling strength at R_h^h stacking. Furthermore, $t_0^{\lambda\xi_\lambda}$ is chosen so that for small θ, the maximum tunneling strength corresponds to the value in the untwisted case. The exponential $e^{-\theta^2/\theta_0^2}$ takes into account the approximate Gaussian increase of the interlayer distance that occurs throughout the supercell. With this effective model for tunneling strength around the Γ valley we have a clear twist angle dependence for the tunneling as can be seen in Fig. 5(c). The evolution of the tunneling strength through the superlattice can be seen in Fig. 5(e), where we see the tunneling strength converging towards the same value $t^\lambda(d_{max})$. All parameters used to model the tunneling around the Γ point in this paper can be found in Tab. S2.

Once the real space map of the the tunneling strength has been obtained (Eq. (3)), the modeled tunneling strength can then be decomposed as a Fourier series

$$t_{l_\lambda l'_\lambda}^{\lambda\xi_\lambda}(\boldsymbol{r}) = \sum_{\boldsymbol{g}} t_{l_\lambda l'_\lambda}^{\lambda\xi_\lambda}(\boldsymbol{g})e^{i\boldsymbol{g}\cdot\boldsymbol{r}}, \tag{4}$$

where $t_{l_\lambda l'_\lambda}^{\lambda\xi_\lambda}(\boldsymbol{g})$ can be calculated by solving the integral Fourier coefficients

$$t_{l_\lambda l'_\lambda}^{\lambda\xi_\lambda}(\boldsymbol{g}) = \frac{1}{\mathcal{A}_M}\int_{\mathcal{A}_M} d\boldsymbol{r}e^{-i\boldsymbol{g}\cdot\boldsymbol{r}}t_{l_\lambda l'_\lambda}^{\lambda\xi_\lambda}(\boldsymbol{r}). \tag{5}$$

Table S2. Parameters for the tunneling strength for holes around the Γ valley. These values correspond to the tunneling strength of the heterostructure MoS_2-WS_2. Note that the tunneling strength does not vary much between different materials and the same qualitative behavior is expected regardless of the material [4].

$t(d_{max})$	t_0	α	β	θ_0^2
216 meV	105 meV	-40 meV	-0.4 meV	30

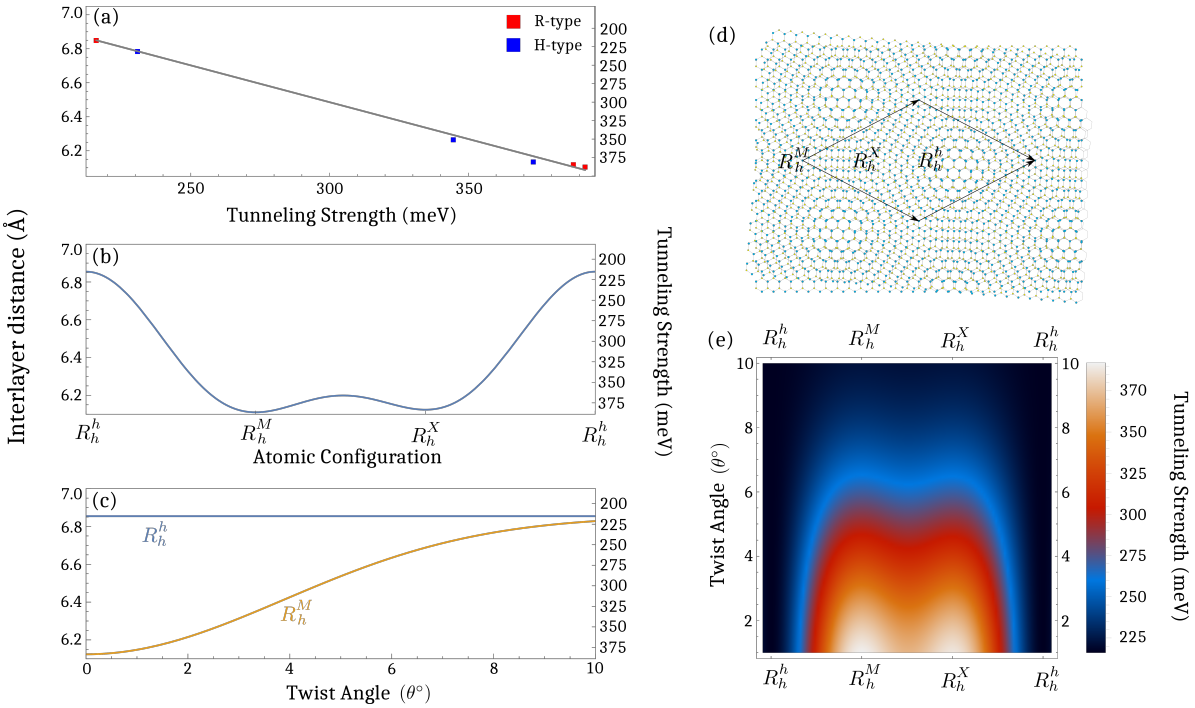

Figure S5. (a) Tunneling strength around the Γ valley as a function of interlayer distance. (b) Interlayer distance (left axis) and tunneling strength around the Γ valley (right axis) in different parts of the superlattice (d). (c) Gaussian increase of interlayer distance as a function of twist angle. Here, we allow the R_h^M configuration to approach the interlayer distance of R_h^h. (e) Evolution of tunneling strength around the Γ valley for different sites in the superlattice when increasing twist angle.

References

[1] Wei-Ting Hsu et al. "Second harmonic generation from artificially stacked transition metal dichalcogenide twisted bilayers". In: *ACS nano* 8.3 (2014), pp. 2951–2958.

[2] Lukas Mennel, Matthias Paur, and Thomas Mueller. "Second harmonic generation in strained transition metal dichalcogenide monolayers: MoS_2, $MoSe_2$, WS_2, and WSe_2". In: *APL Photonics* 4.3 (2019), p. 034404.

[3] Christopher Linderälv et al. "The moiré potential in twisted transition metal dichalcogenide bilayers". In: *arXiv preprint arXiv:2205.15616* (2022).

[4] Joakim Hagel et al. "Exciton landscape in van der Waals heterostructures". In: *Physical Review Research* 3.4 (2021), p. 043217.

[5] Joakim Hagel, Samuel Brem, and Ermin Malic. "Electrical tuning of moiré excitons in $MoSe_2$ bilayers". In: *2D Materials* 10.1 (2022), p. 014013.

[6] Samuel Brem et al. "Tunable phases of moiré excitons in van der Waals heterostructures". In: *Nano letters* 20.12 (2020), pp. 8534–8540.